

MOF-Derived Iron Catalysts for Non-Oxidative Propane Dehydrogenation

Michele L. Sarazen, and Christopher W Jones

J. Phys. Chem. C, **Just Accepted Manuscript** • DOI: 10.1021/acs.jpcc.8b08066 • Publication Date (Web): 27 Nov 2018

Downloaded from <http://pubs.acs.org> on November 28, 2018

Just Accepted

“Just Accepted” manuscripts have been peer-reviewed and accepted for publication. They are posted online prior to technical editing, formatting for publication and author proofing. The American Chemical Society provides “Just Accepted” as a service to the research community to expedite the dissemination of scientific material as soon as possible after acceptance. “Just Accepted” manuscripts appear in full in PDF format accompanied by an HTML abstract. “Just Accepted” manuscripts have been fully peer reviewed, but should not be considered the official version of record. They are citable by the Digital Object Identifier (DOI®). “Just Accepted” is an optional service offered to authors. Therefore, the “Just Accepted” Web site may not include all articles that will be published in the journal. After a manuscript is technically edited and formatted, it will be removed from the “Just Accepted” Web site and published as an ASAP article. Note that technical editing may introduce minor changes to the manuscript text and/or graphics which could affect content, and all legal disclaimers and ethical guidelines that apply to the journal pertain. ACS cannot be held responsible for errors or consequences arising from the use of information contained in these “Just Accepted” manuscripts.



MOF-derived Iron Catalysts for Non-Oxidative Propane Dehydrogenation

Michele L. Sarazen and Christopher W. Jones*

School of Chemical & Biomolecular Engineering
Georgia Institute of Technology
Atlanta, GA 30332

*to whom correspondence should be addressed: cjones@chbe.gatech.edu

Abstract

The dehydrogenation of light alkanes, sourced from cracking of traditional petrochemical feedstocks and from emerging shale gas, represents an attractive route to alkenes (ethene, propene, butenes), which are the building blocks for valuable polymers and chemicals. Carbon-supported iron catalysts formed from pyrolysis of Fe-containing metal organic frameworks (MOFs; Fe-BTC) are investigated here for propane dehydrogenation. The temperature of pyrolysis was found to influence the iron phase (oxide, metal, carbide) and surface area of the material, but the high temperature reduction and reaction conditions needed for PDH (773-873 K) result in a metallic iron phase that is shown to be active and selective for propene formation, though differential isoconversion data indicate the pyrolysis temperature affects the selectivity to propene. X-Ray absorption spectroscopy (XAS) and X-ray diffraction (XRD) are utilized to investigate the catalyst state both pre- and post- reduction and reaction. This work demonstrates how using MOFs as precursors may allow the synthesis of useful and perhaps unique catalyst structures that can be designed to obtain desired rates and product selectivities of hydrocarbon processes.

1. Introduction

Light alkenes (ethene, propene, butenes) are vital building blocks within the chemical industry.¹ The increasing abundance and decreasing price of shale gas in North America provides an attractive alternative to traditional petrochemical feedstocks. If the ethane and propane found in shale gas are utilized in existing cracking technologies (currently based on naphtha), propene production would not meet the current demand. Thus, on-purpose propene production, such as catalytic propane dehydrogenation (PDH), is of interest.

Significant research has focused on catalysts based on Cr and Pt as well as alloys of these metals and other metal oxides.^{2–21} The industrial Cr and Pt catalysts, while being components of highly effective technologies, still have disadvantages such as significant deactivation due to coke formation, which requires intensive catalyst regeneration protocols. The selectivity and stability of catalysts for PDH, in both oxidative and nonoxidative pathways, are pertinent in designing new, less expensive materials because several undesired side reactions like hydrogenolysis, isomerization, and coke formation can occur. Thus, alternative catalysts comprised of non-precious metals that do not compromise reactivity and selectivity but offer increased stability can lead to substantial impact in the field of propene production for PDH due to the large scale needed.

Iron-based catalysts have been demonstrated as potential candidates for PDH, especially for oxidative PDH using various oxidants (O_2 , N_2O , CO_2).^{22–25} Investigations of nonoxidative PDH for iron catalysts have included Fe-substituted ZSM-5,²⁶ Fe_2O_3 supported on sulfated Al_2O_3 ,²⁷ Fe catalysts supported on Al_2O_3 modified with phosphate species,²⁸ and silica supported isolated Fe^{2+} species.²⁹

Recently, a novel method for synthesizing small, relatively uniform iron-based nanoparticles via the pyrolysis of Fe-containing metal organic frameworks (MOFs) has been

1
2
3 reported.³⁰ During pyrolysis, the metal ion nodes migrate to form clusters and the organic linkers
4
5 rearrange to form a carbon shell/support. This method can access various classes of supported iron,
6
7 such as metal, oxide, and carbide (as well as different phases within those subclasses), making
8
9 them attractive for Fischer-Tropsch synthesis, where they have been shown as active and stable
10
11 catalysts at 613 K.^{30–33} The temperature of pyrolysis was found to influence the iron-carbide phase
12
13 and the size of the nanoparticles formed. In this study, we utilize iron-containing MOFs
14
15 (specifically Fe-BTC) as scaffolds to synthesize catalysts for PDH and investigate how these
16
17 materials respond to the higher temperature reaction conditions needed for PDH (773–873 K). We
18
19 have found that the reactivity and selectivity of these MOF derived iron catalysts are dependent
20
21 on the temperature of pyrolysis and reaction and correlate these results to differences in iron
22
23 speciation or structure as determined from various characterization techniques. These MOF-
24
25 derived catalysts represent promising materials for PDH because they are (i) based on a cheaper
26
27 and more abundant metal than current commercial dehydrogenation catalysts, (ii) have high iron
28
29 loadings without compromising surface area, and (iii) do not deactivate (when reduced) as readily
30
31 as other supported dehydrogenation catalysts, due to the carbon shell around the active center.
32
33
34
35
36
37
38
39

40 **2. Experimental Procedures**

41 **2.1 Synthesis of MOF-mediated catalysts (FeC)**

42
43 Fe nanoparticles embedded in a porous carbon matrix were produced by the pyrolysis of
44
45 Fe-BTC (iron-1,3,5-benzenetricarboxylate), which was purchased from Sigma-Aldrich (Basolite
46
47 F-300). Pyrolysis of Fe-BTC was carried out in a quartz tubular reactor (approximately $L = 1.0 \text{ m}$
48
49 $\times \text{ID} = 5.0 \text{ cm}$) located horizontally in a ceramic fiber oven where around 1.0 g of the MOF was
50
51 placed in a quartz crucible and subjected to heat treatment in a nitrogen atmosphere (500 sccm).
52
53
54
55
56
57
58
59
60

1
2
3 The temperature was ramped at 2 °C min⁻¹ to 400, 500, 600, and 700 °C and held for 8 h. Before
4 exposure to ambient conditions, samples were passivated at room temperature by inducing an air
5 leak in the flowing N₂ stream for 2 h. The synthesized catalysts are denoted by “FeC_T,” with T
6 representing the pyrolysis temperature in °C.
7
8
9
10
11

12 2.2 Characterization

13
14 XRD patterns were measured with an X’pert Pro X-ray diffractometer from PANalytical
15 with nickel-filtered Cu K α radiation ($\lambda = 1.5406 \text{ \AA}$), with generator settings of 45 kV and 40 mA.
16
17 A scanning region of 3–100° with a scanning step size of 0.026° was used. Textural properties
18 were determined by N₂ adsorption–desorption isotherms carried out with a Tristar II 3020 from
19 Micromeritics. About 0.1 g of sample was degassed under vacuum and preheated at 120 °C for 12
20 h on a Schlenk line before the measurement. TGA was performed on a Netzsch STA409PG TGA
21 by combustion. Mass loss from 123 to 900 °C under a flow of nitrogen-diluted air was recorded to
22 calculate Fe loading on the carbon-matrix catalysts assuming the Fe₂O₃ phase residual mass. The
23 reducibility of Fe-based catalysts was studied by H₂ temperature-programmed reduction (TPR)
24 with Autochem II Chemisorption Analyzer from Micromeritics. About 0.20 g sample was loaded
25 in a quartz tube and was preheated to 120 °C for 1 h in a 50 sccm Ar flow, followed by cooling to
26 50 °C. Then, 30 sccm of a 10 vol % H₂/Ar was introduced while heating to 900 °C with a ramp of
27 5 °C/min. The signal was recorded by a thermal conductivity detector (TCD). TEM was performed
28 on a FEI Tecnai G2 F30 Transmission Electron Microscope operating at 300 kV. The well -
29 dispersed catalyst suspension in H₂O was dropped onto a Lacey carbon coated copper grid and
30 dried in ambient air for sample preparation.
31
32
33
34
35
36
37
38
39
40
41
42
43
44
45
46
47
48
49
50

51 X-ray absorption spectroscopy was carried out 12-BM-B at the Advanced Photon Source
52 (Argonne National Laboratory) with a Rh focusing mirror and Si <111> monochromator. An iron
53
54
55
56
57
58
59
60

1
2
3 metal foil and third X-ray detector were placed in the beam path beyond the transmission detector
4
5 to allow acquisition of a reference spectrum concurrent with each sample measurement. Use of a
6
7 custom built reactor cell with a six-port sample holder housed within a quartz tube that was sealed
8
9 by Kapton windows and O-rings, allowing multiple samples to be examined by XAS without
10
11 exposure to air. The catalysts were pretreated at 600 °C in 50 sccm 4% H₂/He flow for 1 h followed
12
13 by purging in a 100 sccm He flow for 30 min. For in situ measurements, 50 sccm 3 % C₃H₈/He
14
15 was flowed over pretreated samples at 550 °C for different 3 hours, followed by measurement at
16
17 room temperature. To facilitate data analysis, XANES reference spectra were collected of FeO,
18
19 Fe₃O₄, Fe₂O₃, and bulk Fe₃C. The EXAFS data were processed using Athena software for
20
21 background removal, post-edge normalization and X-ray absorption near edge structure (XANES)
22
23 analysis.
24
25
26
27

28 2.3 Catalytic measurements 29

30
31 Propane dehydrogenation was carried out using a U-shape quartz reactor of ca. 1/8-inch
32
33 diameter and ca. 80 cm length. The catalyst (0.03-0.1 g) was loaded onto a quartz wool bed in air
34
35 at room temperature, and the quartz reactor with catalyst was loaded into a National Electric
36
37 Furnace series FA 120. The catalyst was then purged with N₂ (Airgas, UHP) for 10 min at RT with
38
39 a flow rate of 20 sccm before any temperature ramp. The reactor was then heated to the desired
40
41 temperature at 5 °C/min under either N₂ at 20 sccm or 10 % H₂ in N₂ at 20 sccm, depending on
42
43 whether a reduction step was tested. Once the temperature reached the desired temperature, the H₂
44
45 flow was maintained for 1-3 hours at a flow rate of 20 sccm. Next, the sample was purged with 20
46
47 sccm N₂ for at least 10 min before introduction of the reactant gas (C₃H₈ balanced with N₂). The
48
49 hydrocarbon products as well as H₂ were analyzed via online gas chromatography (Shimadzu GC-
50
51 2014) equipped with a RESTEK Column (Rt-Alumina BOND/Na₂SO₄, 30 m × 0.25 mm × 4 μm),
52
53
54
55
56
57
58
59
60

1
2
3 a flame ionization detector and a thermal conductivity detector. The carbon mass balance was
4
5 calculated for every time point collected.
6
7

8 **3. Results and Discussion**

9 10 3.1 Structural and textural properties of iron catalysts synthesized at different pyrolysis 11 12 temperatures 13

14
15 Pyrolysis of the metal organic frameworks (MOFs) results in a rearrangement of the
16
17 constituent atoms and a collapse of the highly microporous structure, leaving a metal-based
18
19 nanoparticle (in this case, iron) on a carbon support (TEM in Fig. 1). The BET surface areas,
20
21 measured from N₂ physisorption, and the iron-weight loading measured from combustion
22
23 thermogravimetric analysis (TGA) for the as-received, commercially-available Fe-BTC and the
24
25 series of materials synthesized from different pyrolysis temperatures are included in Table 1 (TGA
26
27 curves are shown in Figure 2, while the isotherms are found in the SI (Fig. S1 for samples
28
29 pyrolyzed at 400, 500, 600, and 700 °C)). The synthesized catalysts are denoted by “FeC_T,” with
30
31 T representing the pyrolysis temperature in °C. FeC_400a was synthesized using a smaller vertical
32
33 reactor, while FeC_400 and all other samples were synthesized using a larger horizontal reactor
34
35 with 10x the loaded mass as the smaller reactor. The lower measured surface area and iron loading
36
37 in FeC_400a compared to FeC_400 is consistent with different residence times of the inert gas
38
39 during pyrolysis in the two reactors. These samples indicate that materials processing, via different
40
41 reactor configurations, can lead to different materials, which highlights the challenge of working
42
43 with these decomposition-based catalyst syntheses. The two examples are included here to call
44
45 attention to these differences. The (larger) horizontal reactor was utilized for the majority of the
46
47 samples, as it allowed larger batches to be synthesized.
48
49
50
51
52
53
54
55
56
57
58
59
60

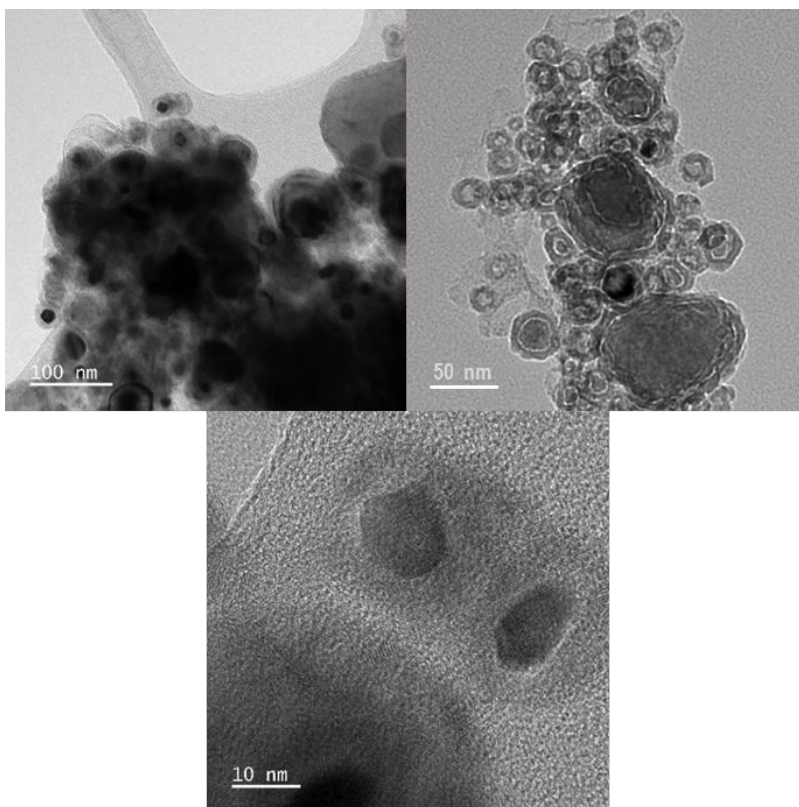


Figure 1. TEM images of FeC₆₀₀ materials at different magnifications.

The iron content was similar (~55 wt. %) for all samples synthesized in the horizontal furnace despite different pyrolysis temperatures (Table 1). The TGA profiles vary, though, as the FeC₆₀₀ and FeC₇₀₀ samples show an increase in mass in the temperature range of 150-500 °C (Fig. 2). The difference between the samples pyrolyzed at the lower temperatures (FeC₄₀₀ and FeC₅₀₀) and those at the higher temperatures (FeC₆₀₀ and FeC₇₀₀) are consistent with the different phases of iron in these materials, as is discussed below with XRD data. The FeC₆₀₀ and FeC₇₀₀ samples are predominately carbidic and metallic iron after pyrolysis, and these species undergo an exothermic phase transition to iron oxide. The measured surface areas for all MOF-derived materials are lower than that of the parent MOF, consistent with the collapse of the ordered microporous structure. The surface area of the FeC_T samples has a maximum in the series for the FeC₆₀₀ sample, corresponding to 310 m²/g. This difference in surface area is indicative of a

carbon support that is more amorphous at lower pyrolysis temperatures, but becomes more ordered as the temperature increases. In fact, a peak appears in the XRD (Fig. 3a) for the FeC₆₀₀ and FeC₇₀₀ samples at 2θ value of ~26°, consistent with the (002) surface of graphite.

Table 1. BET surface area (m²/g) determined from N₂ physisorption and iron weight loading determined from organic TGA (Fig. 2) for as-received Fe-BTC and a series of materials synthesized from different pyrolysis temperatures (T; in °C), where these samples are named by the convention “FeC_T.” FeC_{400a} was synthesized using a vertical reactor; all other samples were synthesized using a horizontal reactor.

| Sample | Fe loading (wt. %) | BET SA (m ² /g) | Pore Volume (cm ³ /g) |
|---------------------|--------------------|----------------------------|----------------------------------|
| Fe-BTC | 20.5 | 830 | - |
| FeC _{400a} | 28.1 | 56 | 0.12 |
| FeC ₄₀₀ | 56.4 | 99 | 0.091 |
| FeC ₅₀₀ | 54.6 | 190 | 0.11 |
| FeC ₆₀₀ | 56.0 | 310 | 0.24 |
| FeC ₇₀₀ | 54.4 | 230 | 0.18 |

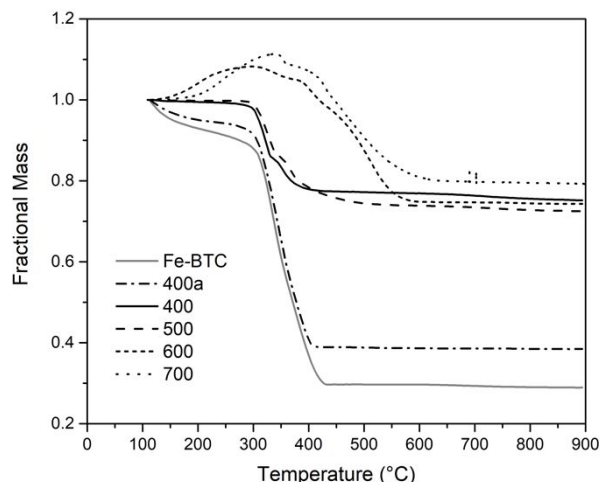


Figure 2. Combustion TGA profiles for as-received Fe-BTC and a series of materials synthesized from different pyrolysis temperatures under flowing N₂. FeC_{400a} was synthesized using a vertical reactor; all other samples were synthesized using a horizontal reactor.

The phase of the iron species was probed using ex-situ XRD after pyrolysis (and a passivation in dilute O₂). Pyrolysis of Fe-BTC at either 400 or 500 °C resulted in predominately

1
2
3 Fe₂O₃, as indicated by simulated XRD reference patterns (Fig. 3b). The relative heights of the
4
5 peaks at 2θ values of 33° and 36°, as well as the small peak at 41°, suggest the presence of FeO.
6
7
8 The multiple peaks centered near 2θ values of 45° for the samples pyrolyzed at 600 and 700 °C
9
10 are consistent with Fe₃C. These phase distributions as a function of temperature are slightly
11
12 different than those reported previously;³¹ specifically, pyrolysis at 600 °C does not result in Fe
13
14 metal. This is most likely due to a difference in pyrolysis reactors, as previously seen within our
15
16 own measurements.
17
18

19
20 The reduction profile of each catalyst was investigated through TPR to gather information
21
22 about the catalyst under an H₂ atmosphere (Fig. 4). The profiles of the catalysts show different
23
24 features, but in general demonstrate a two-step reduction: one at lower temperatures between 200–
25
26 400 °C and one at higher temperatures between 400–750 °C. The low temperature peaks for the
27
28 FeC_400 and FeC_500 samples are consistent with Fe₂O₃ phases reducing to Fe₃O₄/FeO. The
29
30 broad, high temperature peak is associated with the reduction of these iron oxide species to metallic
31
32 Fe.³⁴ The slightly broader first peak and its shift to higher temperatures for the FeC_600 sample
33
34 corresponds to the presence a carbide phase, as evidenced by the TPR profile of bulk Fe₃C (Fig.
35
36 S2). These variances in H₂ uptakes agree with the phases determined by XRD and indicate the
37
38 ability to tune the structural and textural properties via pyrolysis temperature; the effects of these
39
40 changes on the catalytic performance will be addressed next.
41
42
43
44
45
46
47
48
49
50
51
52
53
54
55
56
57
58
59
60

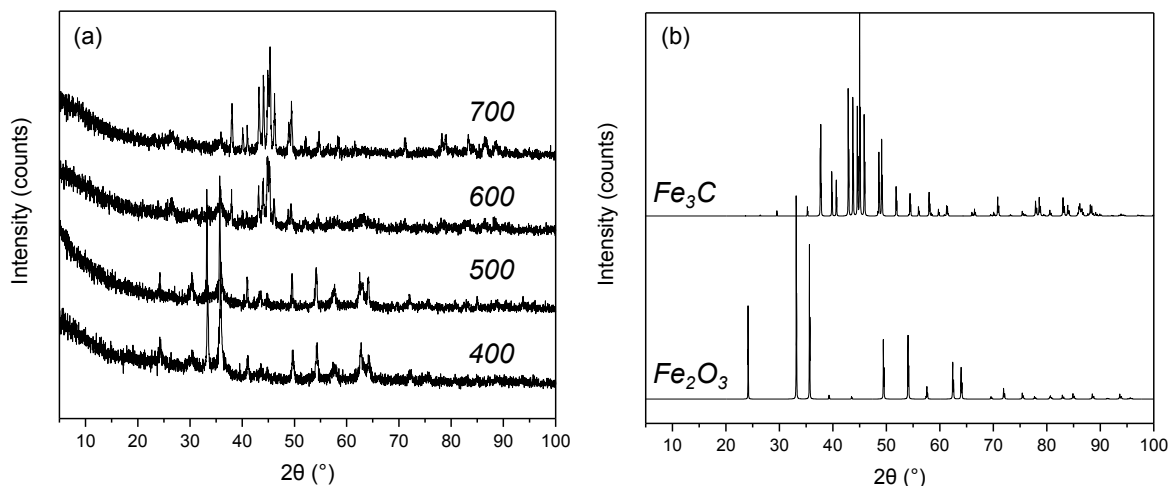


Figure 3. (a) XRD patterns of samples pyrolyzed at 400, 500, 600, and 700 °C and (b) simulated XRD patterns for Fe₂O₃ and Fe₃C.

Figure 4. TPR profiles of each catalysts investigated under an

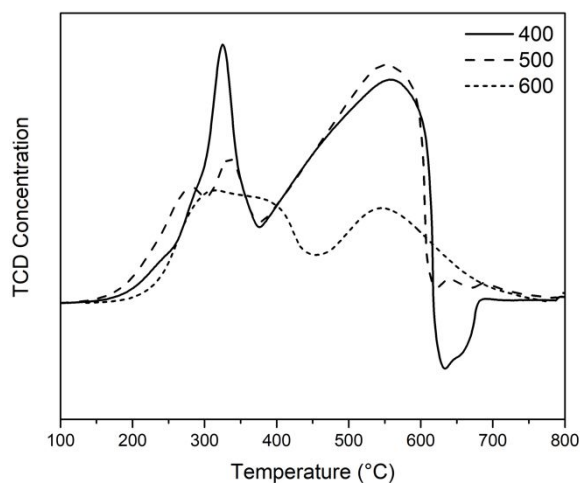


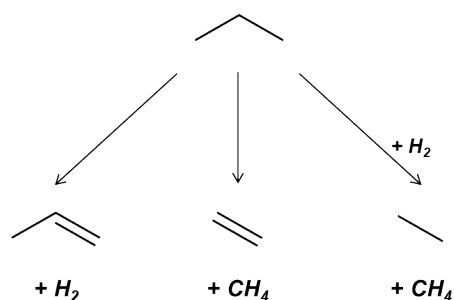
Figure 4. TPR profiles of the FeC_T catalysts in a 10% H₂ (balance Ar) atmosphere with a 500 °C min⁻¹ ramp rate.

3.2 Propane dehydrogenation on MOF-derived iron catalysts

The MOF-derived catalysts were investigated for their reactivity and selectivity during PDH at 550-575 °C (after reduction at 600 °C in H₂). Several side reactions (Scheme 1) can occur at these high temperatures, such as (thermal) cracking to methane and ethene, hydrogenolysis (with the H₂ produced in-situ from dehydrogenation events) to crack to methane and ethane, or coking.

All of these side reactions increase the cost of downstream separation and catalyst regeneration, so mitigating them is key for the practical applicability of a material. The selectivities to these thermal reactions were shown using a blank reactor (Fig. S3), and are different than the measured catalytic selectivities discussed below.

Scheme 1. Reactions of propane at elevated temperatures.



Propane consumption turnover rates (normalized by total Fe) are proportional to propane pressure (Fig. 5a for FeC_600) under differential conditions consistent with a monomolecular surface reaction occurring on the catalyst surface that is void of any reactant or product derived species. This form of a rate expression would also indicate that alkene products do not significantly take place in further surface catalyzed conversion events to high molecular weight molecules, which agrees with the dearth of aromatic species. The selectivity to propene is independent of propane pressure (Fig. S4a), but is dependent on catalyst residence time (Fig. S4b). The selectivity to C₁-C₂ species increases at long residence times, which indicates some pathways for their formation go through a propene derived intermediate. These additional cracking pathways can both be thermal and catalytic. However, Figure 5b shows that, for a given pressure and residence time, the FeC_600 catalyst exhibited stable propene selectivity for ~50 hours, which is desirable. The carbon balance and hydrogen production for this extended run are included in the SI (Fig. S5).

Further, the carbon balance and propene selectivity remain high even at higher conversions (~20 %; Fig. S6).

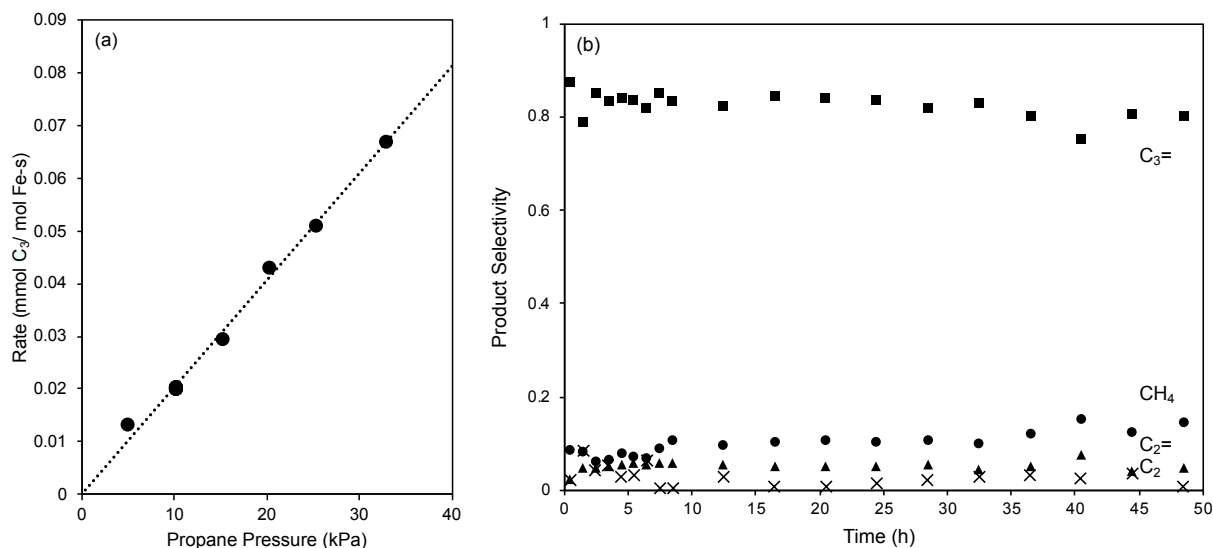


Figure 5. (a) Propane consumption turnover rate (normalized per total mol Fe; a) as a function of propane pressure and (b) product selectivity at 5 kPa C₃H₈ for long times on stream for FeC₆₀₀. Reaction conditions: reduction at 600 °C in 20 sccm H₂ for 10.8 ks; reaction at 550 °C in 0.5-4 sccm C₃H₈ in N₂; 30 mg catalyst (FeC₆₀₀; 55 wt.% Fe).

The performance of the MOF-derived catalysts synthesized using different pyrolysis temperatures was also examined and compared to that of bulk Fe₃C. Figure 6 shows the propene selectivity and the carbon balance at differential isoconversion (5 %) for the FeC_T samples. Propene selectivity increases with increasing pyrolysis temperature, but is similar for FeC₆₀₀ and FeC₇₀₀. The difference in propene selectivity between FeC_{400a} and FeC₄₀₀, 0.38 and 0.61 fractional selectivity, respectively, suggest a concomitant effect of the catalyst surface area, iron weight loading and phase of iron. The carbon balance for the FeC₄₀₀₋₆₀₀ samples is near unity, but decreases for FeC₇₀₀. This carbon is most likely lost as coke deposits on the catalyst surface, which is consistent with the more rapid deactivation on this sample compared to FeC₆₀₀

(Fig. S7). The Fe_3C bulk sample had low propene selectivity and carbon balance, as expected, but was used as a general comparison.

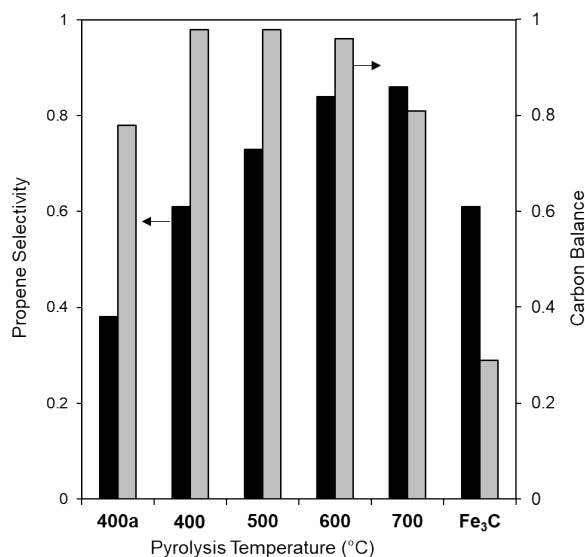


Figure 6. Propene selectivity and carbon balance for the catalyst series and commercially available iron carbide at 3.6 ks of TOS and isoconversion (5 %). Reaction conditions: reduction at 600 °C in 20 sccm H_2 for 10.8 ks; reaction at 550 °C in 5 kPa C_3H_8 (balance N_2).

The structural differences in these materials were discussed in Section 3.1, and their different catalytic activity is evident in Figure 6; thus, XAS was utilized to further probe the catalyst to gain an understanding how and why they behave differently.

3.3 XAS investigation to determine active structure

The MOF-derived catalysts were first reduced under H_2 at 600 °C before reaction. The TPR profiles (Figure 4), along with well-known reducibility of iron, would suggest a metallic-like phase during reaction. Thus, the catalysts were investigated using X-ray absorption spectroscopy (XAS) at the Fe K-edge (ca. 7112 eV) to determine their properties during and after reduction as well as after reaction. In particular, the oxidation state and coordination environment of Fe were characterized by X-ray absorption near edge structure (XANES) and extended X-ray adsorption fine structure (EXAFS), respectively.

The XANES data for FeC_400-600 samples prior to H₂ reduction as well as for the Fe₂O₃ reference are shown in Figure 7a. The pre-edge energy of the 3d orbital transition for the FeC_400-500 samples were similar to that of Fe₂O₃, indicating the presence of Fe(III) species, consistent with the XRD data (Fig. 3a). FeC_600 did not exhibit this distinct pre-edge feature, but instead had a shoulder, which increased in intensity under H₂ with increasing temperature as the white line decreased (Fig. 7b). After H₂ reduction, the pre-edge feature for FeC_400 and FeC_500 disappeared and all materials appeared metallic (Fig. 7c). This reduction of the Fe₃C phase is consistent with ex-situ XRD analysis after reduction of 1 and 3 hours (Fig. S8) and also appears to occur for the FeC_400-500 samples that were initially Fe₂O₃.

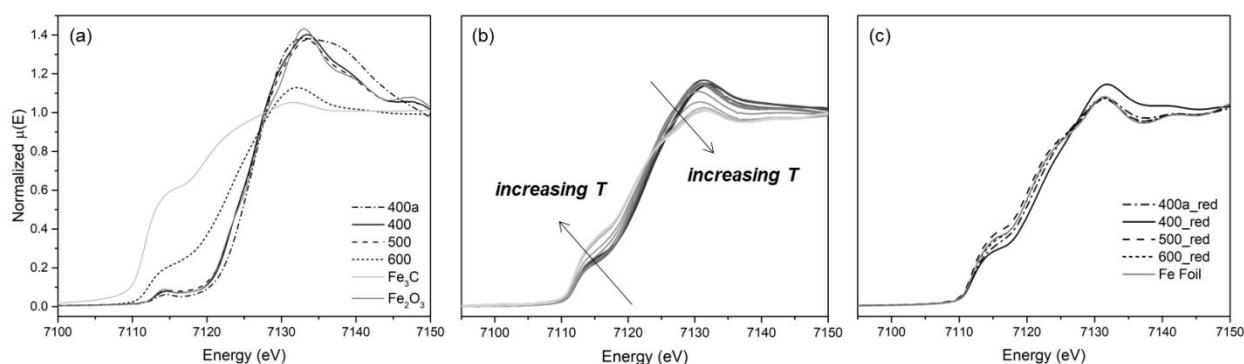


Figure 7. Fe k-edge X-ray absorption near-edge spectroscopy (XANES) spectra of FeC_T samples, bulk Fe₃C, and references (Fe₂O₃ and Fe foil) (a) in He at room temperature before reduction, (b) in H₂ during reduction with increasing temperature (FeC_600), and (c) in He at room temperature after reduction in H₂ for 2.5 hours at 600 °C.

Figure 7a is replotted as Figure 8a to show the direct comparison to the R spaces of the EXAFS spectra for the samples before reduction (Fig. 8b). Before the reduction, the strongest signal for FeC_400-500 samples was at ~1.4 Å, which is associated with the Fe–O bond. This peak disappeared after H₂ pretreatment with a concomitant appearance of a strong peak at ~2.2 Å, indicating the formation of metallic Fe domains and fewer iron oxide species (Fig. S9). FeC_600 had a peak ~1.5 Å before reduction (Fig. 8b), which is characteristic of Fe–C bonds. Further, the

Fe-Fe peak appears at lower radial distances than that in Fe metal. After reduction, this Fe-Fe peak shifts to ~ 2.2 Å and the Fe-C peak disappears. This represents further evidence for the transformation of the precursors to metallic Fe after the high temperature reduction.

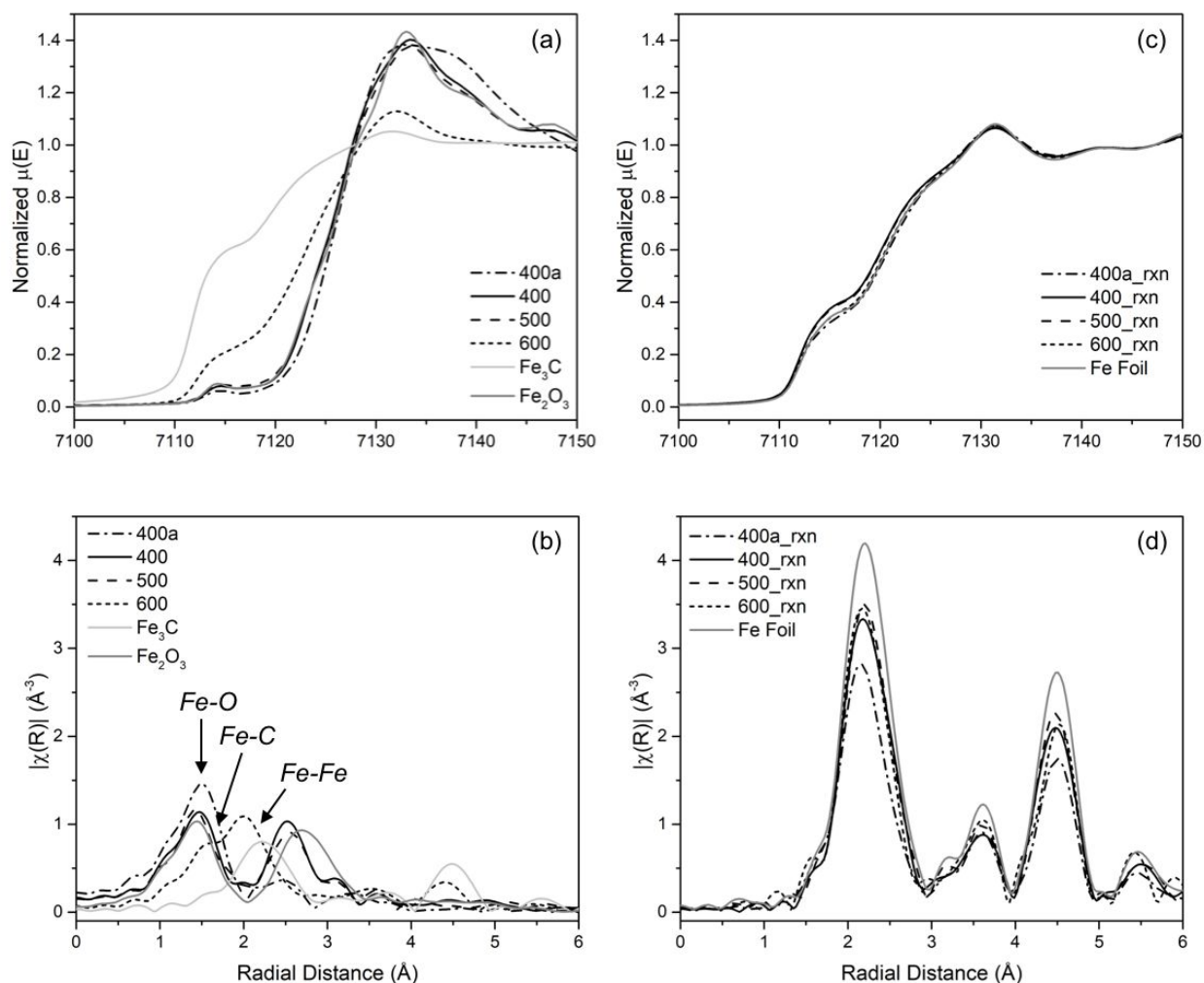


Figure 8. Fe k-edge XANES spectra (a) and magnitude of the Fourier transform of the EXAFS spectra (b) of FeC_T samples, bulk Fe_3C , and references (Fe_2O_3 and Fe foil) in He at room temperature before reduction or reaction. Fe k-edge XANES spectra (c) and magnitude of the Fourier transform of the EXAFS spectra (d) after reduction in H_2 for 2.5 hours at 600 °C and after reaction in 3 kPa C_3H_8 (balance He) for 2 hours at 550 °C.

1
2
3 The XANES data for all samples look similar to each other and similar to the Fe foil after
4 propane dehydrogenation (Fig. 8c), as do the R spaces of the EXAFS (Fig. 8d). Ex-situ XRD
5 patterns of the samples after reaction in a traditional flow reactor also indicate the formation and
6 stability of the metallic Fe phase after reaction (Fig. S10). The only exception is the small feature
7 in the FeC_600 sample after reaction, which is near 1.5 Å and that is attributed to Fe-C. Further,
8 the ex-situ post-reaction XRD for this sample shows a broadening around 2θ values of 45° , which
9 is the region where Fe [110] and Fe₃C peaks overlap; this broadening was not evident in the XRD
10 pattern after reduction. These data suggest that this material may form small carbide domains
11 during reaction. However, the carbon balance as well as the long-term stability do not indicate the
12 deposition of C-atoms from propane or its subsequent products. Thus, a local restructuring of the
13 carbon support and incorporation of these carbon atoms into the nanoparticles could be occurring.
14
15
16
17
18
19
20
21
22
23
24
25
26
27

28 These results indicate the majority of the iron phase in these catalysts remains metallic and
29 selective for PDH, however, iron oxide, metal, carbide all may be active. Prior work by this group²⁸
30 showed that iron-phosphorous pre-catalysts on Al₂O₃ formed Fe₂O₃ (when synthesized in a 3Fe:P
31 ratio), which was converted to metallic iron after reduction in H₂ at 600 °C. Within the first 30
32 minutes of reaction, measured propene formation was low despite propane consumption and
33 hydrogen formation. Ex-situ XRD suggested that Fe₃C was formed and was the more active and
34 stable phase using that catalyst composition. It is postulated that the presence of P and alumina in
35 that case affected the phase stability, whereas the carbon support in this work stabilizes the metallic
36 iron phase. Sustained activity of metallic iron supported on carbon was also demonstrated by others
37 for isobutane dehydrogenation.³⁵
38
39
40
41
42
43
44
45
46
47
48
49
50

51 To further explore the reactivity of different iron domains in these materials, the reactivity
52 of these other iron speciations was tested using the un-reduced materials. As shown in Figure 3
53
54
55
56
57
58
59
60

1
2
3 (and Fig. 7a), these materials are either iron oxide (predominately Fe₂O₃: FeC_400 and FeC_500)
4
5 or iron carbide (FeC_600 and FeC_700). Data from Figure S11 indicate that, while these materials
6
7 do have higher selectivity to propene formation than their reduced analogs, they are not as stable.
8
9 They deactivate significantly even at the differential conditions utilized in these studies, which is
10
11 consistent with a lower carbon balance for all times on stream. These results indicate that multiple
12
13 phases of iron are in fact active for propane dehydrogenation to propene, but materials with
14
15 predominantly metallic iron are the most stable using the catalyst compositions described here.
16
17

18 19 **4. Conclusion**

20
21 Carbon-supported iron catalysts formed from pyrolysis of Fe-containing metal organic
22
23 frameworks (MOFs; Fe-BTC) were investigated for non-oxidative propane dehydrogenation. The
24
25 phase of the supported iron (oxide, metal, carbide) and surface area of the material were affected
26
27 by the temperature of pyrolysis. However, the high temperature reduction and reaction conditions
28
29 needed for PDH (773-873 K) result in a predominantly metallic iron phase, as shown from X-ray
30
31 adsorption spectroscopy (XAS) and X-ray diffraction (XRD), that appears active for propene
32
33 formation. Further, this active catalyst remains stable for propene formation for > 48 hours. This
34
35 work demonstrates how using MOFs as precursors may allow the synthesis of stable catalyst
36
37 structures that can be designed to optimize product selectivities of hydrocarbon processes.
38
39

40 41 42 **5. Acknowledgments**

43
44 We thank Dr. Taylor P. Sulmonetti for many useful discussions and aid in collection XAS data
45
46 and Dr. Kristina Golub for aid in collection of XRD data. This work was financially supported by
47
48 the Love Family Professorship at Georgia Institute of Technology. XAS studies were conducted
49
50 using resources of the Advanced Photon Source, a U.S. Department of Energy (DOE) Office of
51
52 Science User Facility operated for the DOE Office of Science by Argonne National Laboratory
53
54
55
56
57
58
59
60

1
2
3 under Contract No. DE-AC02-06CH11357 with help from Dr. Sungsik Lee (Argonne National
4 Laboratory).
5
6

7 **6. Supporting Information**

8
9
10 Supporting Information Available: N₂ physisorption isotherms, additional TPR profiles and XRD
11 patterns, blank reactor data, residence times and pressure effects on product selectivity, extended
12 reaction time and high conversion reactor data, XAS of samples after reduction, reactor data
13 (carbon balance, conversion, propene selectivity) with or without reduction.
14
15
16

17 This material is available free of charge via the Internet at <http://pubs.acs.org>.
18
19

20 **7. References**

- 21
22
23
24 (1) Sattler, J. J. H. B.; Ruiz-Martinez, J.; Santillan-Jimenez, E.; Weckhuysen, B. M. Catalytic
25 Dehydrogenation of Light Alkanes on Metals and Metal Oxides. *Chem. Rev.* **2014**, *114*,
26 10613–10653.
27
28
29
30
31 (2) Redekop, E. A.; Galvita, V. V.; Poelman, H.; Bliznuk, V.; Detavernier, C.; Marin, G. B.
32 Delivering a Modifying Element to Metal Nanoparticles via Support: Pt–Ga Alloying
33 during the Reduction of Pt/Mg(Al,Ga)O_x Catalysts and Its Effects on Propane
34 Dehydrogenation. *ACS Catal.* **2014**, *4*, 1812–1824.
35
36
37
38
39
40 (3) Sattler, J. J. H. B.; Gonzalez-Jimenez, I. D.; Luo, L.; Stears, B. A.; Malek, A.; Barton, D.
41 G.; Kilos, B. A.; Kaminsky, M. P.; Verhoeven, T. W. G. M.; Koers, E. J.; et al. Platinum-
42 Promoted Ga/Al₂O₃ as Highly Active, Selective, and Stable Catalyst for the
43 Dehydrogenation of Propane. *Angew. Chemie Int. Ed.* **2014**, *53*, 9251–9256.
44
45
46
47
48
49 (4) Zhang, Y.; Zhou, Y.; Zhang, S.; Zhou, S.; Sheng, X.; Wang, Q.; Zhang, C. Catalytic
50 Structure and Reaction Performance of PtSnK/ZSM-5 Catalyst for Propane
51 Dehydrogenation: Influence of Impregnation Strategy. *J. Mater. Sci.* **2015**, *50*, 6457–6468.
52
53
54
55
56
57
58
59
60

- 1
2
3 (5) Childers, D. J.; Schweitzer, N. M.; Shahari, S. M. K.; Rioux, R. M.; Miller, J. T.; Meyer, R.
4
5 J. Modifying Structure-Sensitive Reactions by Addition of Zn to Pd. *J. Catal.* **2014**, *318*,
6
7 75–84.
8
9
10 (6) Zhu, H.; Anjum, D. H.; Wang, Q.; Abou-Hamad, E.; Emsley, L.; Dong, H.; Laveille, P.; Li,
11
12 L.; Samal, A. K.; Basset, J.-M. M. Sn Surface-Enriched Pt-Sn Bimetallic Nanoparticles as
13
14 a Selective and Stable Catalyst for Propane Dehydrogenation. *J. Catal.* **2014**, *320*, 52–62.
15
16
17 (7) Xia, K.; Lang, W.-Z.; Li, P.-P.; Long, L.-L.; Yan, X.; Guo, Y.-J. The Influences of Mg/Al
18
19 Molar Ratio on the Properties of PtIn/Mg(Al)O-X Catalysts for Propane Dehydrogenation
20
21 Reaction. *Chem. Eng. J.* **2016**, *284*, 1068–1079.
22
23
24 (8) Long, L.-L.; Lang, W.-Z.; Yan, X.; Xia, K.; Guo, Y.-J. Yttrium-Modified Alumina as
25
26 Support for Trimetallic PtSnIn Catalysts with Improved Catalytic Performance in Propane
27
28 Dehydrogenation. *Fuel Process. Technol.* **2016**, *146*, 48–55.
29
30
31 (9) Li, P.-P.; Lang, W.-Z.; Xia, K.; Luan, L.; Yan, X.; Guo, Y.-J. The Promotion Effects of Ni
32
33 on the Properties of Cr/Al Catalysts for Propane Dehydrogenation Reaction. *Appl. Catal. A*
34
35 *Gen.* **2016**, *522*, 172–179.
36
37
38 (10) Kang, K. H.; Kim, T. H.; Choi, W. C.; Park, Y.-K.; Hong, U. G.; Park, D. S.; Kim, C.-J.;
39
40 Song, I. K. Dehydrogenation of Propane to Propylene over CrO_y-CeO₂-K₂O/γ-Al₂O₃
41
42 Catalysts: Effect of Cerium Content. *Catal. Commun.* **2015**, *72*, 68–72.
43
44
45 (11) Weckhuysen, B. M.; Schoonheydt, R. A. Alkane Dehydrogenation over Supported
46
47 Chromium Oxide Catalysts. *Catal. Today* **1999**, *51*, 223–232.
48
49
50 (12) Conley, M. P.; Delley, M. F.; Núñez-Zarur, F.; Comas-Vives, A.; Copéret, C. Heterolytic
51
52 Activation of C-H Bonds on Cr^{III}-O Surface Sites Is a Key Step in Catalytic Polymerization
53
54 of Ethylene and Dehydrogenation of Propane. *Inorganic Chemistry* **2015**, *54*, 5065–5078.
55
56
57
58
59
60

- 1
2
3 (13) Hu, B.; “Bean” Getsoian, A.; Schweitzer, N. M.; Das, U.; Kim, H.; Niklas, J.; Poluektov,
4 O.; Curtiss, L. A.; Stair, P. C.; Miller, J. T.; et al. Selective Propane Dehydrogenation with
5 Single-Site CoII on SiO₂ by a Non-Redox Mechanism. *J. Catal.* **2015**, *322*, 24–37.
6
7
8
9
10 (14) Fridman, V. Z. Pathways of Light Compounds Formation during Propane and Isobutane
11 Dehydrogenation on Al-Cr Catalysts. *Appl. Catal. A Gen.* **2010**, *382*, 139–147.
12
13
14 (15) Tan, S.; Gil, L. B.; Subramanian, N.; Sholl, D. S.; Nair, S.; Jones, C. W.; Moore, J. S.; Liu,
15 Y.; Dixit, R. S.; Pendergast, J. G. Catalytic Propane Dehydrogenation over In₂O₃–Ga₂O₃
16 Mixed Oxides. *Appl. Catal. A Gen.* **2015**, *498*, 167–175.
17
18
19
20 (16) Chen, M.; Xu, J.; Liu, Y. M.; Cao, Y.; He, H. Y.; Zhuang, J. H. Supported Indium Oxide as
21 Novel Efficient Catalysts for Dehydrogenation of Propane with Carbon Dioxide. *Appl.*
22 *Catal. A Gen.* **2010**, *377*, 35–41.
23
24
25
26 (17) Santhosh Kumar, M.; Chen, D.; Holmen, A.; Walmsley, J. C. Dehydrogenation of Propane
27 over Pt-SBA-15 and Pt-Sn-SBA-15: Effect of Sn on the Dispersion of Pt and Catalytic
28 Behavior. *Catal. Today* **2009**, *142*, 17–23.
29
30
31
32 (18) Fan, X.; Li, J.; Zhao, Z.; Wei, Y.; Liu, J.; Duan, A.; Jiang, G. Dehydrogenation of Propane
33 over PtSnAl/SBA-15 Catalysts: Al Addition Effect and Coke Formation Analysis. *Catal.*
34 *Sci. Technol.* **2015**, *5*, 339–350.
35
36
37
38 (19) Baek, J.; Yun, H. J.; Yun, D.; Choi, Y.; Yi, J. Preparation of Highly Dispersed Chromium
39 Oxide Catalysts Supported on Mesoporous Silica for the Oxidative Dehydrogenation of
40 Propane Using CO₂: Insight into the Nature of Catalytically Active Chromium Sites. *Acs*
41 *Catal.* **2012**, *2*, 1893–1903.
42
43
44
45 (20) Gallagher, J. R.; Childers, D. J.; Zhao, H.; Winans, R. E.; Meyer, R. J.; Miller, J. T.
46 Structural Evolution of an Intermetallic Pd-Zn Catalyst Selective for Propane
47
48
49
50
51
52
53
54
55
56
57
58
59
60

- 1
2
3 Dehydrogenation. *Phys. Chem. Chem. Phys.* **2015**, *17*, 28144–28153.
4
5
6 (21) Sattler, J. J. H. B.; Mens, A. M.; Weckhuysen, B. M. Real-Time Quantitative Operando
7
8 Raman Spectroscopy of a CrOx/Al₂O₃ Propane Dehydrogenation Catalyst in a Pilot-Scale
9
10 Reactor. *ChemCatChem* **2014**, *6*, 3139–3145.
11
12 (22) Bulánek, R.; Wichterlová, B.; Novoveská, K.; Kreibich, V. Oxidation of Propane with
13
14 Oxygen And/or Nitrous Oxide over Fe-ZSM-5 with Low Iron Concentrations. *Appl. Catal.*
15
16 *A Gen.* **2004**, *264*, 13–22.
17
18 (23) Kondratenko, E. V.; Pérez-Ramírez, J. Oxidative Functionalization of Propane over FeMFI
19
20 Zeolites: Effect of Reaction Variables and Catalyst Constitution on the Mechanism and
21
22 Performance. *Appl. Catal. A Gen.* **2004**, *267*, 181–189.
23
24
25 (24) Michorczyk, P.; Kuśtrowski, P.; Chmielarz, L.; Ogonowski, J. Influence of Redox
26
27 Properties on the Activity of Iron Oxide Catalysts in Dehydrogenation of Propane with
28
29 CO₂. *React. Kinet. Catal. Lett.* **2004**, *82*, 121–130.
30
31
32 (25) Michorczyk, P.; Ogonowski, J. Dehydrogenation of Propane in the Presence of Carbon
33
34 Dioxide over Oxide-Based Catalysts. *React. Kinet. Catal. Lett.* **2003**, *78*, 41–47.
35
36
37 (26) Yun, J. H.; Lobo, R. F. Catalytic Dehydrogenation of Propane over Iron-Silicate Zeolites.
38
39 *J. Catal.* **2014**, *312*, 263–270.
40
41
42 (27) Sun, Y.; Wu, Y.; Shan, H.; Wang, G.; Li, C. Studies on the Promoting Effect of Sulfate
43
44 Species in Catalytic Dehydrogenation of Propane over Fe₂O₃/Al₂O₃ Catalysts. *Catal. Sci.*
45
46 *Technol.* **2015**, *5*, 1290–1298.
47
48
49 (28) Tan, S.; Hu, B.; Kim, W.-G.; Pang, S. H.; Moore, J. S.; Liu, Y.; Dixit, R. S.; Pendergast, J.
50
51 G.; Sholl, D. S.; Nair, S.; et al. Propane Dehydrogenation over Alumina-Supported
52
53 Iron/Phosphorus Catalysts: Structural Evolution of Iron Species Leading to High Activity
54
55
56
57
58
59
60

- 1
2
3 and Propylene Selectivity. *ACS Catal.* **2016**, *6*, 5673–5683.
- 4
5 (29) Hu, B.; Schweitzer, N. M.; Zhang, G.; Kraft, S. J.; Childers, D. J.; Lanci, M. P.; Miller, J.
6
7 T.; Hock, A. S. Isolated Fe^{II} on Silica as a Selective Propane Dehydrogenation Catalyst.
8
9 *ACS Catal.* **2015**, *5*, 3494–3503.
- 10
11 (30) Santos, V. P.; Wezendonk, T. A.; Jaén, J. J. D.; Dugulan, A. I.; Nasalevich, M. A.; Islam,
12
13 H. U.; Chojecki, A.; Sartipi, S.; Sun, X.; Hakeem, A. A.; et al. Metal Organic Framework-
14
15 Mediated Synthesis of Highly Active and Stable Fischer-Tropsch Catalysts. *Nat. Commun.*
16
17 **2015**, *6*, 6451.
- 18
19 (31) Wezendonk, T. A.; Santos, V. P.; Nasalevich, M. A.; Warringa, Q. S. E.; Dugulan, A. I.;
20
21 Chojecki, A.; Koeken, A. C. J.; Ruitenbeek, M.; Meima, G.; Islam, H.-U.; et al. Elucidating
22
23 the Nature of Fe Species during Pyrolysis of the Fe-BTC MOF into Highly Active and
24
25 Stable Fischer–Tropsch Catalysts. *ACS Catal.* **2016**, *6*, 3236–3247.
- 26
27 (32) Wezendonk, T. A.; Warringa, Q. S. E.; Santos, V. P.; Chojecki, A.; Ruitenbeek, M.; Meima,
28
29 G.; Makkee, M.; Kapteijn, F.; Gascon, J. Structural and Elemental Influence from Various
30
31 MOFs on the Performance of Fe@C Catalysts for Fischer–Tropsch Synthesis. *Faraday*
32
33 *Discuss.* **2017**, *197*, 225–242.
- 34
35 (33) Wezendonk, T. A.; Sun, X.; Dugulan, A. I.; van Hoof, A. J. F.; Hensen, E. J. M.; Kapteijn,
36
37 F.; Gascon, J. Controlled Formation of Iron Carbides and Their Performance in Fischer-
38
39 Tropsch Synthesis. *J. Catal.* **2018**, *362*, 106–117.
- 40
41 (34) Jozwiak, W. K.; Kaczmarek, E.; Maniecki, T. P.; Ignaczak, W.; Maniukiewicz, W.
42
43 Reduction Behavior of Iron Oxides in Hydrogen and Carbon Monoxide Atmospheres. *Appl.*
44
45 *Catal. A Gen.* **2007**, *326*, 17–27.
- 46
47 (35) Shimada, H.; Akazawa, T.; Ikenaga, N. O.; Suzuki, T. Dehydrogenation of Isobutane to
48
49
50
51
52
53
54
55
56
57
58
59
60

1
2
3 Isobutene with Iron-Loaded Activated Carbon Catalyst. *Appl. Catal. A Gen.* **1998**, *168*,
4
5 243–250.
6
7
8
9
10
11
12
13
14
15
16
17
18
19
20
21
22
23
24
25
26
27
28
29
30
31
32
33
34
35
36
37
38
39
40
41
42
43
44
45
46
47
48
49
50
51
52
53
54
55
56
57
58
59
60

TOC Image

